



HAL
open science

Imaging a near-surface feature using cross-correlation analysis of multi-channel surface wave data

Kevin Samyn, Adnand Bitri, Gilles Grandjean

► **To cite this version:**

Kevin Samyn, Adnand Bitri, Gilles Grandjean. Imaging a near-surface feature using cross-correlation analysis of multi-channel surface wave data. *Near Surface Geophysics*, 2013, 11 (1), pp.1-10. 10.3997/1873-0604.2012007 . hal-00687133

HAL Id: hal-00687133

<https://brgm.hal.science/hal-00687133>

Submitted on 12 Apr 2012

HAL is a multi-disciplinary open access archive for the deposit and dissemination of scientific research documents, whether they are published or not. The documents may come from teaching and research institutions in France or abroad, or from public or private research centers.

L'archive ouverte pluridisciplinaire **HAL**, est destinée au dépôt et à la diffusion de documents scientifiques de niveau recherche, publiés ou non, émanant des établissements d'enseignement et de recherche français ou étrangers, des laboratoires publics ou privés.

16

17 **Abstract**

18 In this study, we demonstrate that cross-correlation gathers of multi-channel
19 and multi-shot configurations provide accurate estimations of shear wave
20 velocity (V_S) perturbations from Rayleigh wave data for the reconstruction of
21 two-dimensional (2D), high-resolution velocity distributions without requiring the
22 systematic calculation of surface wave dispersions, as in the spectral analysis
23 of surface waves (SASW). Data acquisition for cross-correlation analysis is
24 similar to that for a 2D seismic common midpoint reflection survey. The data
25 processing involved is similar to the coda wave interferometry used for
26 seismological data but differs in the sense that the cross-correlation of the
27 original waveform is calculated for active source seismic data. Data processing
28 in cross-correlation analysis consists of the following three steps: First, cross-
29 correlations are calculated for every trace in each shot gather with the same
30 offset trace as a reference shot to flatten the linearly sloping events of surface
31 waves. A common receiver location stack section can then be obtained, which
32 allows for the assessment of lateral variations in the elastic properties of the
33 medium. Second, the maxima of the time-shifted cross-correlation gathers and
34 the maxima of the shot gathers' envelope traces are picked for different
35 frequencies, and trace values having the same receiver location are averaged
36 to calculate V_S perturbations, as described in the theory of coda wave
37 interferometry. Finally, a 2D V_S profile is reconstructed by applying the lateral
38 V_S perturbation to a homogeneous V_S velocity profile obtained by inversion of
39 the surface wave dispersion of the reference shot gather. Analyses of waveform

40 data from numerical modelling and field observations indicate that this new
41 method is valid and greatly improves the accuracy and resolution of near-
42 surface imagery using surface waves and reconstructed subsurface velocity
43 distributions compared with a conventional SASW or multi-channel application.

44

45 **Keywords**

46 surface wave, cross-correlation, shear-wave velocity (V_s)

47

48 **Introduction**

49

50 The delineation of shear wave velocity (V_s) structures down to a depth of
51 approximately 30 m is of fundamental interest in engineering and environmental
52 problems. P-wave and S-wave (PS) velocity logging has been adopted for this
53 purpose for a number of years. The expense of drilling a borehole and operating
54 a logging tool has led to a demand for more convenient methods for
55 determining shallow surface wave structures. It is well known that the dispersion
56 of the phase velocities of surface waves is mainly determined by the ground
57 structure. The use of surface waves for near-surface delineation has been the
58 subject of many studies in the past decade. For example, the spectral analysis
59 of surface waves (SASW) has been used for the determination of 1D V_s
60 structures down to a depth of 100 m (Nazarian *et al.* 1983; Stokoe *et al.* 1989;
61 Grandjean and Bitri 2006). The majority of the surface wave methods described
62 to date employ a shaker or a vibrator as a wave source and exploit calculated
63 phase differences between two receivers using a simple cross-correlation
64 technique. Park *et al.*, 1998a and Debeglia *et al.* (2006) also discuss the
65 feasibility of detecting near-surface features using dynamic linear moveout
66 (dlmo) for surface wave imagery. A multi-channel analysis of surface waves
67 (MASW) has been proposed by several authors (Song *et al.* 1989; Park *et al.*
68 1999a; Xia *et al.* 1999). This method determines phase velocities directly from
69 multi-channel surface wave data after applying an integral transformation to the
70 frequency-domain waveform data. The integration directly converts time-domain
71 waveform data (time-distance) into an image of phase velocity versus frequency

72 (c-f). Hayashi *et al.* (2004) show that the accuracy and resolution of (c-f)
73 images can be improved using common mid-point (CMP) cross-correlation
74 analysis of multi-channel surface wave data. The MASW method is more
75 effective than the SASW method because MASW allows the fundamental mode
76 of Rayleigh wave dispersion to be distinguished visually from body waves and
77 from higher modes of the Rayleigh waves. Additionally, the MASW method
78 avoids spatial aliasing, which is a problem in the SASW method (Foti *et al.*
79 2001; Neducza 2007). Xia *et al.* (2005) and Miller *et al.* (1999) applied the
80 MASW method to continuous-profiling shot records and delineated 2D Vs
81 structures and their resolution to determine phase velocities at low frequencies.
82 Importantly, Park *et al.* (1999a) noted that it is essential for the MASW method
83 to use a receiver array that is as long as is practical. However, a longer receiver
84 array can decrease the lateral resolution of a survey because the conventional
85 MASW method provides a velocity model averaged over the total length of the
86 array. We developed a novel method to address this trade-off. Developing an
87 alternative to conventional surface wave methods for the determination of
88 lateral variations in Vs structure required a unique approach based on the multi-
89 channel recording of surface waves and a cross-correlation analysis.

90

91 **Surface wave response to a near-surface feature**

92

93 A near-surface anomaly is defined here as a component of the near-surface
94 materials that has elastic properties differing significantly from those of the

95 remaining components, which are termed normal zones. The transition from a
96 normal to anomalous zone may be either abrupt or gradual. During a surface
97 waves survey, a near-surface anomaly leaves a signature of its presence in
98 several forms on a multi-channel recording, the most common form being
99 different phase velocities for those frequencies propagating through or near the
100 anomaly; another form consists of differing attenuation characteristics.

101 In addition to differing phase velocities and attenuation characteristics, an
102 anomaly may reveal its presence in the form of the generation of higher modes
103 (Bath 1973; Gucunski and Woods 1991), or reflected and diffracted
104 (Yanovskaya 1989; Sheu *et al.* 1988) surface waves. The generation of these
105 higher modes is closely related to the existence of a low-velocity zone underlain
106 by and overlying high-velocity zones (a zone of velocity inversion) (Stokoe *et al.*
107 1994), and the energy of the higher modes typically becomes more significant
108 at high frequencies (short wavelengths) (Tokimatsu *et al.* 1992). Reflected and
109 diffracted surface waves are generated when the transition from normal to
110 anomalous zones is abrupt. All of these anomaly signature types may appear
111 on a multichannel record when either the source or the receivers are located at
112 or near the surface location of an anomaly.

113 Theoretically, surface waves cannot penetrate through a void filled with air or
114 fluid because of the lack of shear modulus inside the void. However,
115 considering the retrograde elliptical motion of mass underneath a roll
116 disturbance, the surface waves that penetrate above and below the void with
117 dimensions of elliptical motion that significantly exceed the dimensions of the

118 void may still propagate horizontally but with altered propagation characteristics
119 with respect to attenuation, variations in phase velocity, or both.

120

121 **Methodology**

122

123 *Principles*

124

125 To improve the lateral resolution of multichannel surface wave methods, we
126 considered the Vs perturbation relative to a reference shot gather through the
127 cross-correlation of Rayleigh wave shot gather data recorded at different
128 positions along a line. Cross-correlation is a standard method of estimating the
129 degree to which two series are correlated. The cross-correlation function, $R(\Delta t)$,
130 represents the correlation coefficient between two seismic signals at time $t = 0$,
131 $S(0)$, and a later time t , $S(t)$. The cross-correlation function can be expressed as
132 follows:

$$133 \quad R(\Delta t) = \frac{\sum_{i=0}^{M-m} S_1(i\tau)S_2(i\tau + m\tau)}{\langle S_1 \rangle \langle S_2 \rangle (M - m)} \quad (1)$$

134 where m is an integer multiple of a time interval, τ , such that $\Delta t = m\tau$ (where
135 $0 < m < M$). $S_1(t)$ and $S_2(t)$ are the time-dependant surface wave signals from
136 traces 1 and 2, respectively. Both traces comprise $M+1$ data points spanning
137 the period from $t=0$ to $t=M\tau$. $\langle S_1 \rangle$ and $\langle S_2 \rangle$ are the mean intensities of the
138 surface wave signal in traces 1 and 2, respectively.

139 Herein, we compare the surface wave signals. Our goal is to determine whether
140 the two signals are correlated (i.e., fluctuating in concert) or uncorrelated
141 (fluctuating independently). In modelling the autocorrelation in time, we assume
142 that the correlation of a surface wave signal with itself decays from a perfect
143 correlation at time zero to no correlation at infinite time. For the cross-
144 correlation between two surface wave signals at different locations, assuming
145 seismic source repeatability, near-surface features and near-surface Vs
146 structures create perturbations, and the two signals then fluctuate
147 independently; thus, the correlation between them decays at a certain
148 propagation time.

149 Cross-correlation temporally correlates the intensity fluctuations of the seismic
150 traces. In cross-correlation, only pairs of coherent samples from two distinct
151 traces appear as a positive result at time t , whereas fluctuations in the surface
152 wave signal created by a Vs perturbation generate a positive result at time $t+dt$,
153 accounting for the travel-time perturbation dt .

154 On a simplistic level, cross-correlation analysis is coincidence analysis. The
155 cross-correlation function between traces therefore enables a determination of
156 the manner in which the Vs structure varies in the near surface.

157

158 *Data processing procedure*

159

160 A cross-correlation analysis of surface waves (CCASW) is applied to each shot
161 gather in the dataset. Data acquisition for the CCASW method is similar to that

162 for a 2D seismic common midpoint reflection survey. The source-receiver
163 geometry is based on the end-on spread, and both the source and the receivers
164 move up along a survey line. The processing for the CCASW is summarised in
165 the following:

166 First, cross-correlations are calculated for every trace in each shot gather along
167 the entire seismic line using the same offset trace of a user-selected reference
168 shot gather from the overall dataset, which is considered to be unperturbed.
169 The reference location is a presumably normal zone within the survey line. The
170 cross-correlation process allows us to correct for the offset effect and therefore,
171 to flatten the linearly sloping events of surface waves in the same way as a
172 dlmo (Park *et al.* 1998a, b). All of the common receiver location traces in cross-
173 correlated shot gathers can then be stacked together. The above procedure
174 achieves the following effects after stacking:

- 175 • Frequencies that have the same phase velocity as that at the reference
176 location will have large stacked amplitudes due to constructive interference.
- 177 • For those shot gathers obtained at or near the surface location of an anomaly,
178 cross-correlation will result in time-shifted stacked traces or weak amplitudes
179 traces due to destructive interference.
- 180 • All of the higher modes will be attenuated through destructive interference due
181 to their different phase velocities.
- 182 • All non-planar, body waves will be attenuated due to destructive interference
183 because of their nonlinear occurrence on a multi-channel record or because of
184 wrong velocities used for moveout correction.

- 185 • All reflected surface waves will appear as diffractions in the final stack section.
186 • Random noise will be attenuated.

187 When the stacked traces are displayed, all of the normal zones will show large
188 amplitudes, and the anomalous zones will be denoted by diffractions,
189 attenuated amplitudes or time-shifted events. Such a stack section is thus a
190 good method to obtain an initial view of the lateral variations in elastic properties
191 along the survey line.

192 To quantify the observations made on the stack section, we then applied coda
193 wave interferometry to our active source survey, stipulating that a
194 homogeneous relative change in seismic velocity, dv/v , results in a time-shift dt
195 (Snieder *et al.* 2002; Wegler and Sens-Schönfelder 2006) of:

196
$$dt = -t \frac{dv}{v} \quad (2)$$

197 For this purpose, the maxima of the cross-correlated gather is then picked to
198 obtain the travel-time perturbation dt , and the maxima of the shot gather's
199 envelope traces are used to obtain the surface wave travel time, t . The trace
200 envelope is an attribute of seismic traces computed using the function
201 `suattributes` of the Seismic Unix (SU) package and corresponds to the envelope
202 amplitude of the trace.

203 These two variables are inserted into equation (2) to calculate the Vs
204 perturbations dv/v . The Vs perturbations with the same receiver location are
205 averaged. A Vs profile is reconstructed by applying the velocity perturbation

206 model at different frequencies to a homogeneous V_s profile obtained by
207 inversion of the surface wave dispersion of the reference shot gather.

208

209 **Numerical modelling**

210

211 Two numerical tests were performed to evaluate the proposed method. Fig. 1
212 shows the source-receiver configuration used for data acquisition. Fig. 2 shows
213 the velocity models used for numerical modelling. Both directions of the moving-
214 source observations of surface waves on the survey line were tested. The two
215 models are composed of a homogeneous half-space with $V_p=1200$ m/s and
216 $V_s=600$ m/s and a low-velocity, vertical and buried defect with $V_p=1000$ m/s
217 and $V_s=500$ m/s. The Seismic Unix (SU) `suea2df` function (Juhlin, 1995), which
218 is based on a stress-velocity, staggered grid, 2D finite-difference method
219 (Levander, 1988; Virieux, 1986), was used for the waveform calculation.
220 Synthetic seismic gathers were generated using a zero-phase Ricker wavelet.
221 The finite difference calculation was performed using 321 and 213 0.5×0.5 m
222 cells, respectively, for the x and z axes and 12000 samples with a sample
223 interval of 0.1 ms. The synthetic model size was chosen to be sufficiently large
224 to get free from border effects. After the calculations, the data were resampled
225 to 48 traces with 1 m spacing and 1000 samples with a 1 ms sample interval
226 and processed using CCASW.

227 Fig. 3 presents a flow diagram illustrating the processing procedure for the
228 synthetic shot gather data obtained through numerical modelling. Fig. 3a

229 illustrates the cross-correlation operation for selected synthetic examples. The
230 variables dt , t , and dv/v are highlighted in Figure 3b.

231 Figs. 4a, 4b, and 4c show the resultant stack section and calculated Vs
232 perturbation (dv/v) for the vertical defect synthetic model. Evident velocity
233 perturbation artefacts appear on both sides of the perturbation peak according
234 to the direction of the moving-source observation. In fact, when the source
235 location is centred on the position of the defect, the waveform is perturbed for
236 all the shot gathers even when some traces lie outside of the anomaly. To
237 remedy this phenomenon, only the maxima of both calculated Vs perturbations
238 (dv/v) of the two moving-source datasets are retained. Fig. 4c shows that the
239 value of dv/v around -20% obtained from CCASW of the whole seismic line is
240 coherent with the inferred true Vs perturbation value of -17%, which provides a
241 consistency check for the method.

242 To characterise the in-depth velocity perturbation, a zero-phase, sine-squared,
243 tapered band-pass filter centred on the frequencies 10 Hz to 45 Hz, in
244 increments of 5 Hz, was applied after the cross-correlation analysis. The
245 variables dt and t were then obtained for different frequencies of the surface
246 wave. A “pseudo-depth” for the calculated dv/v was retrieved considering the
247 approximation of the half wavelength of the surface wave (Wightman *et al.*
248 2003):

$$249 \quad d = 0.53 \frac{V_{ph}}{f} \quad (3)$$

250 where d is the depth, V_{ph} is the phase velocity of the surface wave, and f is the
251 frequency. Fig. 5 shows the 2D V_s profiles reconstructed by applying the
252 calculated lateral velocity perturbation (dv/v) to the homogeneous half space.
253 Here, we observe that the CCASW allows for the reconstruction of the synthetic
254 velocity models used for numerical modelling, and that the buried low-velocity
255 defect is resolved using the frequency-depth conversion approximation.

256

257 **Field test: Detection of a buried pipe**

258

259 *Data acquisition*

260

261 Rayleigh wave shot gathers were acquired along a linear profile over a known
262 buried pipe. To increase the speed and efficiency of the data recording and
263 thereby reduce acquisition costs, a multichannel seismic cable was designed
264 and manufactured with 24 takeouts at fixed intervals of 2 m. Each takeout is
265 attached to a single self-orientating, gimballed, vertical geophone with a
266 resonance frequency of 10 Hz. To ensure proper coupling, each gimballed
267 geophone is housed in a heavy casing (~1 kg). To damp the motion of the
268 sensor around its rotational axis, the inside of the casing is filled with viscous
269 oil. The seismic cable was towed behind a vehicle. A 24-channel seismograph
270 was used to record the impacts of a weight-drop electronic seismic source. The
271 source-to-nearest-receiver offset was 2 m, whereas the source stations were
272 separated by 10 m along the survey line. In this way, measurements were

273 performed with a recovering distance, as shown in Fig. 1, between each
274 position of the seismic antenna (meaning that consecutive shots have several
275 common geophones) to improve the signal-to-noise ratio in the CCASW stack
276 section.

277

278 **Field test: Detection of a buried karst**

279

280 *Geological setting*

281

282 As a feasibility test of the previously outlined method, an experiment was
283 conducted to detect a near-surface buried karst as an anomaly. The geological
284 information is provided by 3 the geotechnical soundings performed on the
285 investigation site (Fig. 6a):

286 – The levee embankment consists of loamy materials and brown silt. This
287 formation extends vertically from the surface to a depth around 4–5 m.

288 – A sedimentary formation is represented by the Loire River sandy
289 alluviums and gravels. This formation extends vertically from depths between
290 4–5 m to 12–13 m.

291 The bedrock formation is composed of differentially weathered white limestone
292 and marls that extend to a depth around 13 m. The presence of such easily
293 dissolved bedrock (limestone and dolomite) near the ground surface is
294 characteristic of karst terrain. Because carbonate rocks can be dissolved by

295 groundwater, karst areas are often characterised by sinkholes, springs, and
296 underground streams whereby some surface flows are lost to groundwater
297 (Waltham *et al.* 2005; Halbecq 1996).

298

299 *Data acquisition*

300

301 Rayleigh wave shot gathers were acquired along a linear profile at the top of a
302 flood-protection levee along the Loire River in France (Fig. 6a). The survey site
303 was located in a karst terrain near an area of surface collapses (Fig. 6b), which
304 are among the known subsidence features of karst activity (Waltham *et al.*
305 2005; Halbecq 1996). The purpose of the survey was to detect potential buried
306 karstic features at the location of the collapse. The configuration used for this
307 field test is the same as that used for the detection of the buried pipe and for the
308 karst investigation in Debeglia *et al.* (2006); Which one gave good results in
309 detecting karstic features to a depth around 15-20 m Simultaneously, 3
310 geotechnical soundings (S1, S2, and S3) were performed with the aim of
311 verifying the validity and accuracy of the CCASW method.

312

313 **Results**

314

315 *Detection of a buried pipe*

316

317 A prerequisite to the application of the CCASW to field data was the
318 identification of a reference shot gather that was representative of an
319 unperturbed area for the survey line. The first shot gather was selected for the
320 reference as it was situated at a location where no buried pipe was indicated on
321 the pipeline plan. A CCASW stack section was then computed and a
322 conventional dlmo processing (Park *et al.*, 1998a,b) was also applied to the
323 entire field surface wave dataset for comparison. Fig. 7 shows the comparison
324 between the dlmo stack section (Fig. 7a) and the CCASW stack section (Fig.
325 7b). The buried pipe is revealed as a diffraction at $X=70$ m on both stack
326 sections. The apex of the diffraction appears at the time 0.1 s. Here, we see
327 that the CCASW better resolves the diffraction and allows for improved
328 accuracy and resolution compared with conventional dlmo imagery.

329

330 *Detection of a buried karst*

331

332 A prerequisite to the application of the CCASW to field data was the
333 identification of a reference shot gather that was representative of an
334 unperturbed area for the survey line. This selection was realised using the
335 shape of the phase-velocity-versus-frequency (c - f) dispersion images. The c - f
336 images of the shot gathers located near ($X=280$ m) and far ($X=50$ m) from the
337 collapse ($X=290$ m) were then compared for this purpose. The c - f image of the
338 shot gather located near the collapse (Fig. 8b) exhibited the generation of
339 higher propagation modes, whereas this was not the case for the shot gather

340 located far from the collapse (Fig. 8a). As noted previously, the generation of
341 higher modes is a good indicator of the presence of a complex medium lying
342 below the surface location of the seismic antenna. For this field test, and in
343 many cases, we admit that the generation of higher modes in the c-f image of a
344 shot gather is an inadequate criterion for the choice of this shot gather as a
345 reference. The shot gather at location $X=50$ m was thus selected as the
346 reference shot for the study. Fig. 9 shows a shot gather located at $X=100$ m,
347 away from the collapse, a shot gather located at 280 m, and the respective
348 results of cross-correlation with the reference shot gather. A perturbation can be
349 distinguished near the collapse on the basis of the time-shifted cross-correlation
350 (approximately 0.02 s), whereas no consequent time shift is observed far from
351 the perturbed area. CCASW processing was applied to the entire field surface
352 wave dataset after a zero-phase, sine-squared, tapered band-pass filtering
353 centred on the frequencies 8 Hz to 40 Hz every 2 Hz.

354 We note that this study was conducted in the operational context of a project
355 aimed at assessing Loire River levee integrity over a total distance of
356 approximately 70 km, and we thus did not acquire surface wave data in the two
357 directions of the moving source observation. The calculated V_s perturbations
358 (dv/v) are then likely to be somewhat distorted compared with their true values
359 due to the effects of moving-source artefacts, as illustrated in Fig. 4.
360 Nevertheless, based on the numerical modelling results, we suggest that the
361 general distribution of velocity perturbations constitutes a reasonable first-order
362 approximation of the actual situation in the subsurface. Fig. 10 presents the
363 resulting calculated V_s perturbation (dv/v) for the 16 Hz frequency. Here, a V_s

364 perturbation (dv/v) of approximately -25% appears between the locations at 250
365 m and 300 m and almost centred on the location of the surface collapse. The
366 frequency-depth conversion was then applied using the half-wavelength
367 approximation, and a 2D Vs cross-section was reconstructed by applying the
368 lateral velocity perturbations to a 1D Vs profile obtained by a non-linear least-
369 squares inversion (Xia *et al.* 1999) of the reference shot gather dispersion
370 curve. To ensure the correctness of reference shot gather's inversion, the
371 authors paid attention to the fit between the observed and computed dispersion
372 fundamental curves as in common practice in surface wave methods. A
373 conventional MASW processing with fundamental mode inversion was also
374 applied to the entire field surface wave dataset for comparison. Following the
375 convention, the inverse results for each shot gather were located at the mid-
376 point of each position of the seismic antenna. To assess the lateral variations of
377 elastic properties with depth, the CCASW stack section was convolved with a
378 32-s linear sweep with frequencies decreasing from 40 to 5 Hz. This operation
379 has the effect of separating the different frequencies of the surface wave. The
380 frequency depth conversion was then applied using the half-wavelength
381 approximation.

382 Figs 11a, 11b and 11c show the CCASW stack section and Vs profiles obtained
383 from the MASW and the CCASW methods. The weathering index (*A-value*)
384 curves obtained from the geotechnical soundings are superimposed on the
385 resulting sections. This geotechnical parameter is defined as follows (Pfister
386 1985):

$$387 \quad A = 1 + \left[\frac{POi}{PO \max} - \frac{VAi}{VA \max} \right] \quad (4)$$

388 where POi is the pressure on the drilling tool for depth i , $POmax$ is the maximum
389 pressure on the drilling tool during the sounding, VAi is the velocity of the drilling
390 tool as it progresses in the ground for depth i , and $VAmax$ is the maximum
391 velocity of the progress of the drilling tool during the sounding; A -values vary
392 between 0 for voids and 2 for highly competent materials. A coherent, weak-
393 amplitude, low-velocity anomaly (140–300 m/s) that trends north-west from 0 to
394 23 m depth is evident on the convolved CCASW stack and the CCASW Vs
395 profile and is almost centred on the location of the surface collapse ($X=300$ m)
396 (Fig. 11). The attenuation area is likely caused by destructive interference due
397 to the generation of higher modes near the location of the collapse (Fig. 8b).
398 The anomaly decreases in coherence and magnitude down to a depth of 30 m.
399 It is evident that the shape of the anomaly is roughly consistent with the low to
400 very low A -values (0–1) from the S2 and S3 soundings, revealing the presence
401 of highly deconsolidated materials. The A -values from S1, showing no dramatic
402 values (>1) of the weathering index, reveal the relative competency of the
403 adjacent areas. The MASW Vs profile shows a vast zone with a lower Vs
404 (approximately 450 m/s) between the depths of 20 and 40 m and a vertical shift
405 related to the collapsing feature (Fig. 11b). This shift is likely due to the change
406 in the shape of the fundamental mode in the $c-f$ image, which trends towards
407 lower velocities in the perturbed area compared with the reference $c-f$ image
408 (Fig. 8). Further the velocity depression of the fundamental mode due to the
409 presence of weathered materials, generated higher modes reveal the

410 complexity of the area near the collapse. Nevertheless, the velocity distribution
411 obtained using the MASW does not coincide very well with the *A-value* curves,
412 especially in the 10–20 m depth interval.

413

414 **Discussion**

415

416 The geology of the studied area consists of a levee embankment (brown silt)
417 above a sedimentary formation that is composed of gravels and sand based on
418 a white limestone bedrock. The CCASW stack section and CCASW Vs profile
419 respectively reveal a weak amplitude and low velocities (approximately 140–
420 300 m/s) in an area between 0 and 23 m deep at the location $X=300$ m, likely
421 representing the complexity of the unconsolidated near surface weathered
422 materials. The model presents significantly higher velocities in the adjacent
423 areas. The low field velocities in the CCASW Vs profile likely result from the
424 presence of a karstic collapse below a northwest-trending epikarst created by
425 the flow of sediments into the karstic cavity. The MASW Vs profile shows poor
426 agreement with the actual situation of the subsurface given by the *A-value*
427 curves, indicating that the CCASW method greatly improves upon the accuracy
428 and resolution of the reconstructed subsurface Vs distribution compared with
429 the conventional surface wave methods with fundamental mode inversion.
430 However, we note that this study considers only the fundamental mode and that
431 the MASW Vs profile resolution could be improved when considering the recent
432 achievements in the accurate assessment of Vs profiles using surface wave

433 methods. For example, further studies should compare the results of the
434 CCASW method with the multimode inversion results of *c-f* images or joint
435 inversion using the effective dispersion of surface waves (Hamimu *et al.* 2010).

436

437 **Conclusions**

438

439 The study presents the CCASW method, a novel approach to seismic imaging
440 based on the cross-correlation analysis of multi-channel surface wave data.
441 This method allows for high-resolution surface wave imagery and the accurate
442 estimation of V_s perturbations and enables the reconstruction of two-
443 dimensional subsurface V_s distribution with high resolution without requiring the
444 systematic processes of multichannel spectral analysis of surface waves: the
445 computation of dispersion images and the picking and inversion of dispersion
446 curves. The overall performance of the newly developed method in this study,
447 demonstrates that it is a simple, reliable, and very sensitive technique for
448 characterising lateral variations in near-surface mechanical properties. This
449 method should be applicable to the detection of a variety of subsurface defects
450 (e.g., voids, karsts, or structural heterogeneities). The applicability of this model
451 extends to the characterisation of material properties, integrity assessment, and
452 surface profiling in many types of geotechnical and environmental studies. Our
453 analyses of waveform data derived from numerical modelling and field
454 observations indicate that the CCASW method is valid as an operational
455 sounding method and provides strong inputs for characterisation studies of

456 near-surface features that allow for improved accuracy and resolution compared
457 with conventional surface wave methods.

458

459 **Acknowledgements**

460

461 The study was financed by the French Research and Environment ministry. The
462 authors thank the technicians of the BRGM for acquiring the seismic data.
463 Finally, the authors thank the *Near Surface Geophysics* Editors, Barbara Luke
464 and an anonymous reviewer for their comments and suggestions that led to a
465 much-improved manuscript.

466

467 **References**

- 468 Bath, M. 1973. *Introduction to seismology*. John Wiley and Sons, New York.
- 469 Debeglia N., Bitri A. and Thierry P. 2006. Karst investigations using microgravity
470 and MASW; Application to Orléans, France. *Near Surface Geophysics* 4, 215-
471 225.
- 472 Foti, S., Lancellotta, R., Socco, L. V. and Sambuelli, L. 2001. Application of FK
473 analysis of surface waves for geotechnical characterization. Fourth International
474 Conference on Recent Advances in Geotechnical Earthquake Engineering and
475 Soil Dynamics and Symposium in Honor of Professor W. D. Liam Finn, San
476 Diego, California, March 26-31, 2001.
- 477 Grandjean, G. and Bitri, A. 2006. 2M-SASW: inversion of local Rayleigh wave
478 dispersion in laterally heterogeneous subsurfaces: application to Super-Sauze
479 landslide (France). *Near Surface Geophysics*,4, 215-225.
- 480 Gucunski, N. and Woods, R. D. 1991. Instrumentation for SASW testing In:
481 *Geotechnical Special Publication No. 29, Recent Advances in Instrumentation,*
482 *Data Acquisition and Testing in Soil Dynamics* (eds. S. K. Bhatia and G. W.
483 Blaney), pp. 1-16. American Society of Civil Engineers.
- 484 Halbecq, W. 1996. *Approche géomorphologique des brèches dans les levées*
485 *de la Loire (Geomorphologic approach of breaches in Loire levees)*. Phd thesis.
486 Orléans, Université d'Orléans.(in French).
- 487 Hamimu, L., Safani, J. and Nawawi, M. 2010. Improving the accurate
488 assessment of a shear-wave velocity reversal profile using joint inversion of the

489 effective Rayleigh wave and multimode Love wave dispersion curves. Near
490 Surface Geophysics 9, 1-14.

491 Hayashi, K. and Suzuki, H. 2004. CMP cross correlation analysis of multi-
492 channel surface wave data. Exploration Geophysics 2004 35, 7-13.

493 Juhlin, C. 1995. Finite-difference elastic wave propagation in 2D heterogeneous
494 transversely isotropic media. Geophysical Prospecting 43(6), 843-858.

495 Levander, A.R. 1988. Fourth-order finite-difference P-SV seismograms:
496 Geophysics 53, 1425–1436.

497 Miller, R.D., Xia, J., Park, C.B. and Ivanov, J.M. 1999. Multichannel analysis of
498 surface waves to map bedrock: The Leading Edge 18, 1392–1396.

499 Nazarian, S., Stokoe, K.H. and Hudson, W.R., 1983. Use of spectral analysis of
500 surface waves method for determination of moduli and thickness of pavement
501 system. Transportation Research Record 930, 38–45.

502 Neducza, B. 2007. Stacking of surface waves, Geophysics 72, V51.

503 Park, C. B., Miller, R. D., and Xia, J., 1998a, Ground roll as a tool to image
504 near-surface anomaly:, Society Of Exploration Geophysicists, Annual Meeting
505 Abstracts, 874-877.

506 Park, C.B., Miller, R.D. and Xia, J. 1998b, Imaging dispersion curves of surface
507 waves on multi-channel record:, Society Of Exploration Geophysicists, Annual
508 Meeting Abstracts, 1377-1380.

509 Park, C.B., Miller, R.D. and Xia, J., 1999a, Multimodal analysis of high
510 frequency surface waves. In: *Proceedings of the Symposium on the Application*
511 *of Geophysics to Engineering and Environmental Problems '99*, pp. 115–121.

512 Park, C.B., Miller, R.D. and Xia, J. 1999b, Multichannel analysis of surface
513 waves. *Geophysics* 64, 800–808.

514 Pfister, P. 1985. Recording drilling parameters in ground engineering. *Ground*
515 *Engineering* 18(3), 16–21.

516 Sheu, J.C., Stokoe II, K.H. and Roesset, J.M. 1988. Effect of reflected waves in
517 SASW testing of pavements. *Transportation Research Record No. 1196*, 51-61.

518 Snieder. R., Grêt, A., Douma, H. and Scales, J. 2002. Coda wave
519 interferometry for estimating nonlinear behavior in seismic velocity, *Science*
520 295, 2253–2255.

521 Song, Y.Y., Castagna, J.P., Black, R.A. and Knapp, R.W. 1989. Sensitivity of
522 near-surface shear-wave velocity determination from Rayleigh and Love waves.
523 Technical program with Biographies, SEG, 59th Annual Meeting, Dallas, TX,
524 509-512.

525 Stokoe II, K.H., Wright, G.W., James, A.B. and Jose, M.R. 1994.
526 Characterization of geotechnical sites by SASW method. In: *Geophysical*
527 *characterization of sites, ISSMFE Technical Committee #10* (ed. R.D. Woods),
528 Oxford Publishers, New Delhi.

529 Stokoe II, K.H., Rix, G.J. and Nazarian, S. 1989. In situ seismic testing with
530 surface wave. In: *Proceedings of the XII International Conference on Soil*
531 *Mechanics and Foundation Engineering*, pp. 331-334.

532 Tokimatsu, K., Tamura, S. and Kojima, H. 1992. Effects of multiple modes on
533 Rayleigh wave dispersion characteristics. *Geotechnical Engineering* 118(10),
534 1529-1543.

535 Virieux, J., 1986. P-SV wave-propagation in heterogeneous media: velocity-
536 stress finite-difference method. *Geophysics* 51, 889-901.

537 Xia, J., Miller, R.D. and Park, C.B. 1999. Estimation of near-surface shear-wave
538 velocity by inversion of Rayleigh waves. *Geophysics* 64, 691-700.

539 Xia, J., Chen, C., Tiang, G., Miller, R.D. and Ivanov, J. 2005. Resolution of high-
540 frequency Rayleigh-wave data. *Journal of Environmental and Engineering*
541 *Geophysics* 10(2), 99-110.

542 Waltham, T., Bell, F.G., Culshaw, M.G. 2005. *Sinkholes and Subsidence, Karst*
543 *and Cavernous Rocks in Engineering and Construction Series*. Springer, UK.

544 Wegler, U. and Sens-Schönfelder, C. 2006. Fault zone monitoring with passive
545 image interferometry. *Geophysical Journal International* 168, 1028-1033.

546 Wightman, W.E., Jalinoos, F., Sirles, P. and Hanna, K. 2003. Application of
547 Geophysical Methods to Highway Related Problems. Federal Highway
548 Administration, Central Federal Lands Highway Division, Lakewood, CO,
549 Publication No. FHWA-IF-04-021.

550

551 Yanovskaya, T.B. 1989. Surface waves in media with weak lateral
552 inhomogeneity. In: *Modern approaches in geophysics vol. 9, Seismic surface*
553 *waves in a laterally inhomogeneous earth* (ed. V.I. Keilis-Borok), pp. 35-70.

554

555 **Figure captions**

556

557 **Fig. 1** The source-receiver geometry used in the numerical tests. Both
558 directions of the moving-source observation of surface waves were tested. The
559 shot positions for the gathers shown in Fig. 3 are highlighted.

560

561 **Fig. 2** The V_s models used for the numerical tests. The locations of the seismic
562 antenna for the gathers shown in Fig. 3 are highlighted.

563

564 **Fig. 3** A diagram illustrating the processing of surface wave data. a) Examples
565 of the calculation of cross-correlations from the traces of a perturbed and an
566 unperturbed shot gather with the same offset trace of the reference shot gather.
567 In the unperturbed case, the cross-correlations are centred on the time 0 s. In
568 the perturbed case, the cross-correlations show a travel-time perturbation of
569 approximately 0.01 s. b) Illustration of the calculation of the V_s perturbation
570 (dv/v) using equation (2) and the variables dt and t , which are highlighted by
571 white dotted and solid lines, respectively. In the perturbed case, the V_s
572 perturbation is approximately -10% between traces 30 and 48.

573

574 **Fig. 4** a) A left-right moving source CCASW stack section for the vertical defect
575 model. b) The calculated V_s perturbations (dv/v) for both moving-source
576 directions. Velocity perturbation artefacts appear on the sides of the
577 perturbation peak; c) The calculated V_s perturbation (dv/v) using only the

578 maxima of the calculated dv/v of the two moving-source datasets. The black
579 solid line marks the real velocity perturbation of the model.

580

581 **Fig. 5** The V_s profiles obtained by CCASW processing of the data obtained
582 through numerical modelling of the synthetic models shown in Fig. 2. The
583 locations of the seismic antenna for the gathers shown in Fig. 3 are highlighted.

584

585 **Fig. 6** a) An aerial photograph of the survey site. The black solid line denotes
586 the seismic survey line near the Loire River (France). The red dots mark the
587 locations of the geotechnical soundings (S1, S2 and S3). b) A photograph of the
588 collapse at the top of the flood-protection levee.

589

590 **Fig. 7.** A comparison of the a) dlmo stack section and b) CCASW stack section
591 computed for field data recorded over the buried pipe. Here, we see that the
592 diffraction due to the buried pipe is better resolved by the CCASW stack
593 section.

594

595 **Fig. 8** A comparison of the c - f images of shot gathers located a) far from ($X=50$
596 m) and b) near ($X=280$ m) the collapse ($X=290$ m). The reverse triangle marks
597 the location of the surface collapse, and the black solid and black dotted lines
598 respectively indicate the fundamental and higher propagation modes of the
599 surface waves. The c - f image of the shot gather located near the collapse
600 exhibits the generation of higher propagation modes, although this is not the

601 case for the shot gather located far from the collapse. The shot gather at X=50
602 m was selected as the reference shot for the study. The shot positions of the
603 gathers shown in Fig. 9 are highlighted.

604

605 **Fig. 9** The calculation of cross-correlations from traces of the unperturbed shot
606 gather (located at X=100 m) and the perturbed shot gather (located at X=280 m,
607 near the location of the collapse at X=290 m) with the same offset trace from
608 the reference shot gather (located at X=50 m). In the unperturbed case, the
609 cross-correlations are centred on the time 0 s. In the perturbed case, the cross-
610 correlations show a travel-time perturbation of approximately 0.02 s.

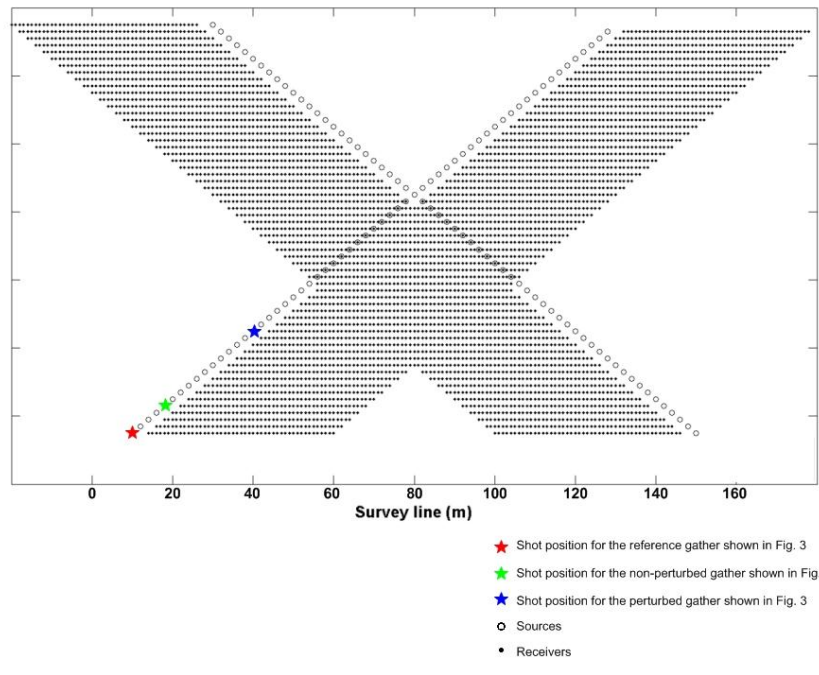
611

612 **Fig. 10** The calculation of Vs perturbations (dv/v) using Equation (2) for the
613 entire field surface wave dataset and for the 16 Hz frequency. A Vs perturbation
614 of approximately -20% appears in the area surrounding the collapse.

615

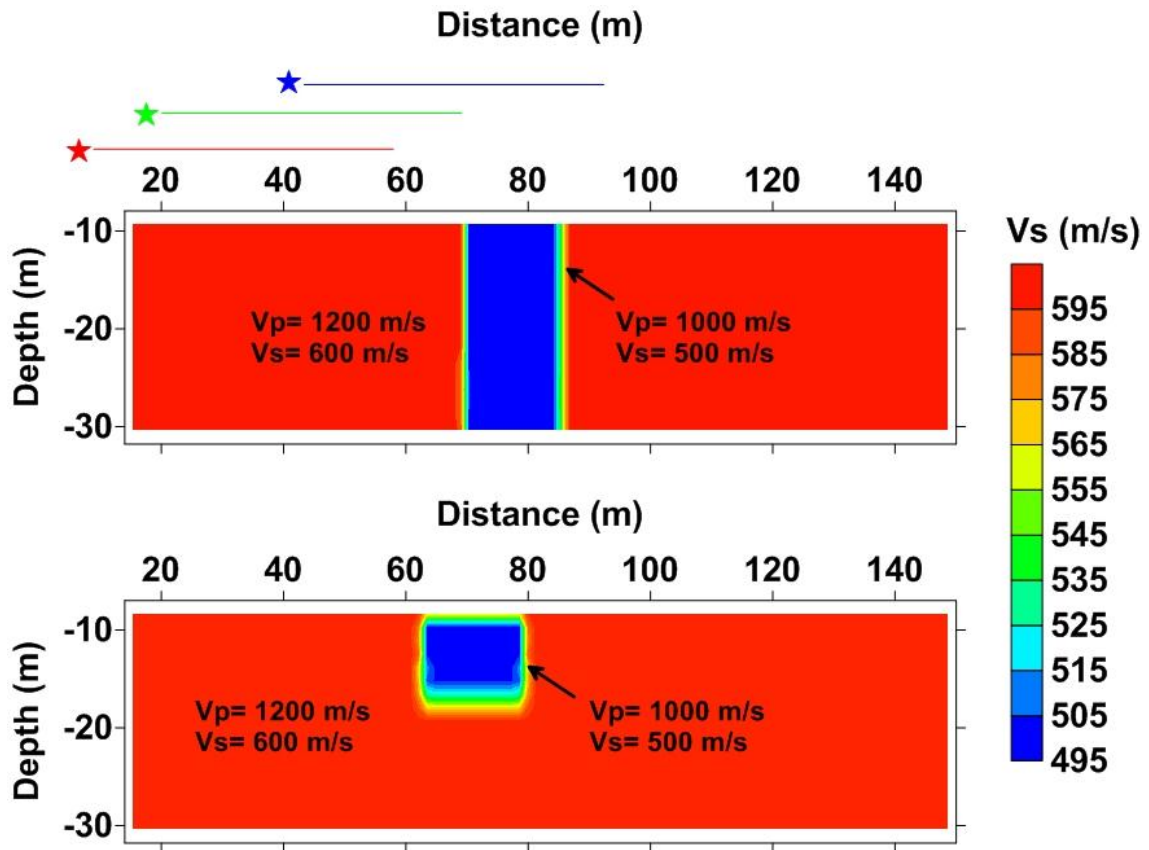
616 **Fig. 11** a) The convolved CCASW stack section. b) Vs profile defined by the
617 MASW method. c) Vs profile defined by the CCASW method. The *A-value*
618 curves overlay the profiles as solid black lines. The triangle marks the location
619 of the surface collapse. The area of attenuated amplitudes in the convolved
620 CCASW stack section is outlined by the dotted black line overlaying the Vs
621 profiles. Here, it is evident that the shape of the weak-amplitude area on the
622 CCASW stack section matches well with the low-velocity anomaly in the
623 CCASW Vs profile.

624



625

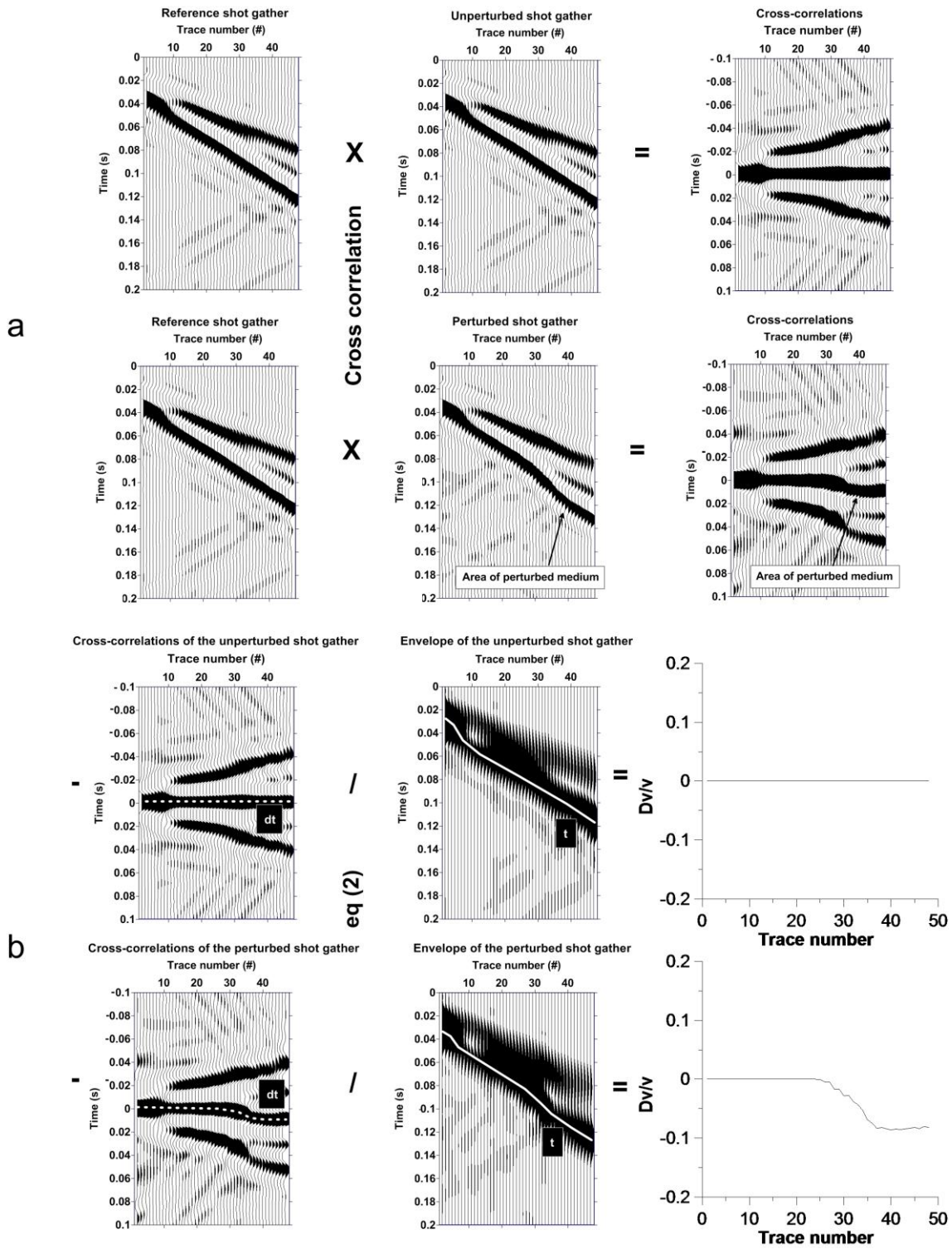
626 Figure. 1



- ★ — Location of the seismic antenna for the reference shot gather shown in Fig. 3
- ★ — Location of the seismic antenna for the non-perturbed shot gather shown in Fig. 3
- ★ — Location of the seismic antenna for the perturbed shot gather shown in Fig. 3

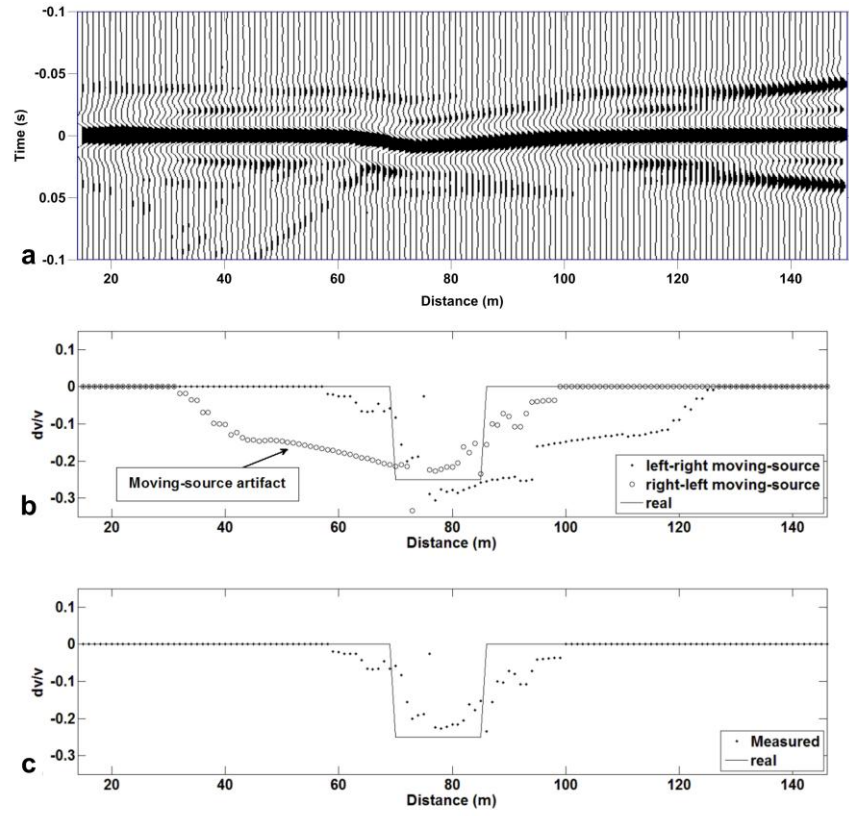
627

628 Figure. 2



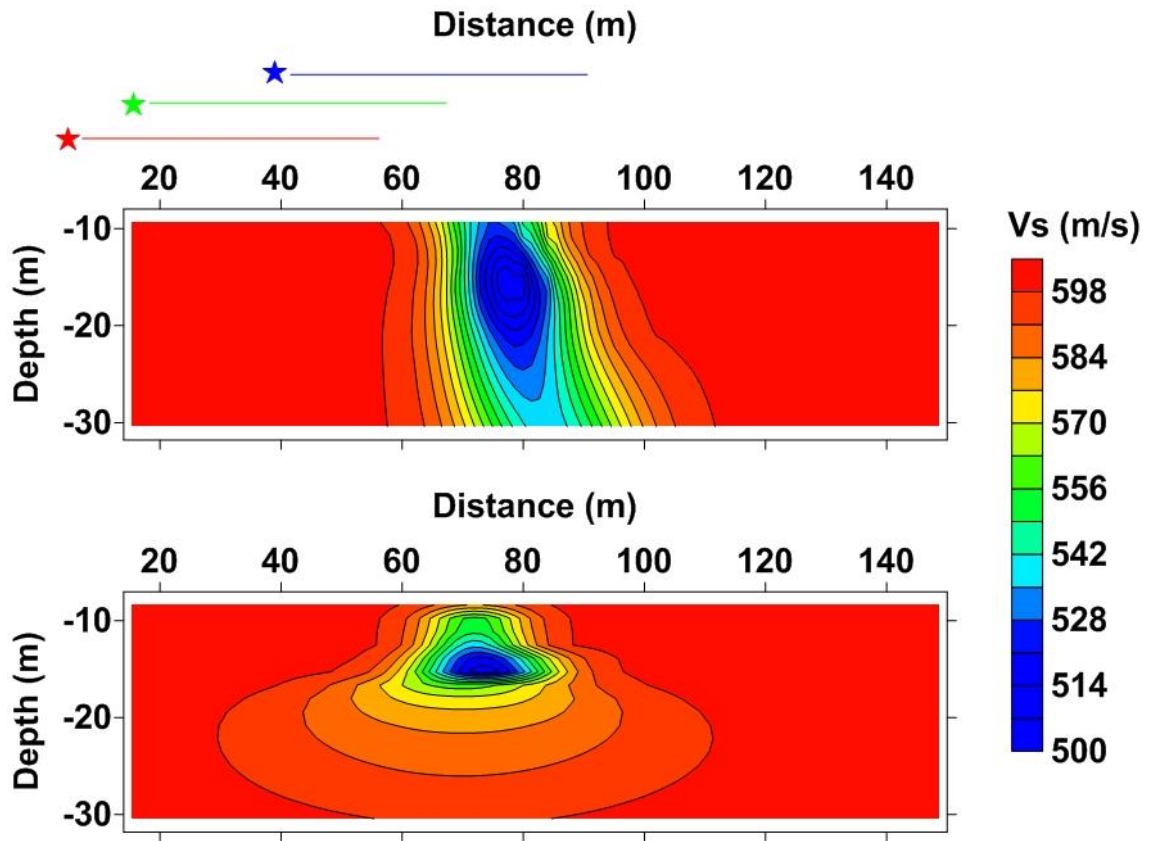
629

630 Figure. 3



631

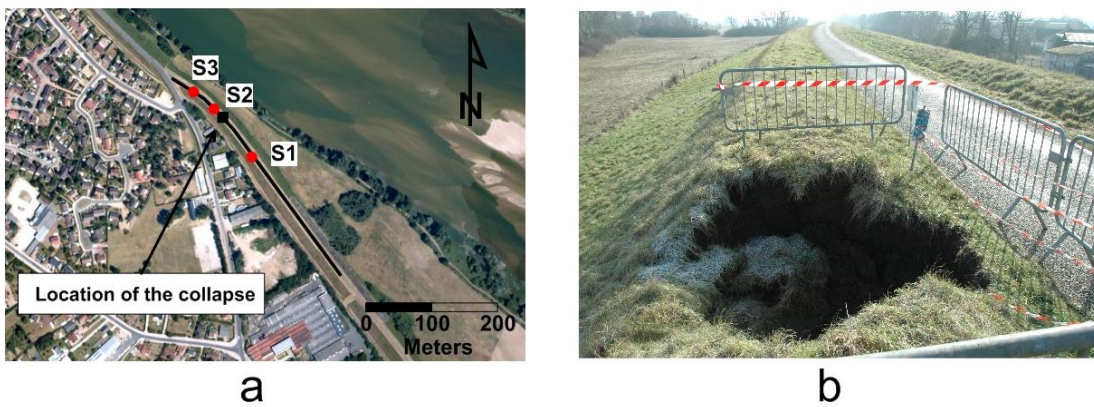
632 Figure. 4



- ★ — Location of the seismic antenna for the reference shot gather shown in Fig. 3
- ★ — Location of the seismic antenna for the non-perturbed shot gather shown in Fig. 3
- ★ — Location of the seismic antenna for the perturbed shot gather shown in Fig. 3

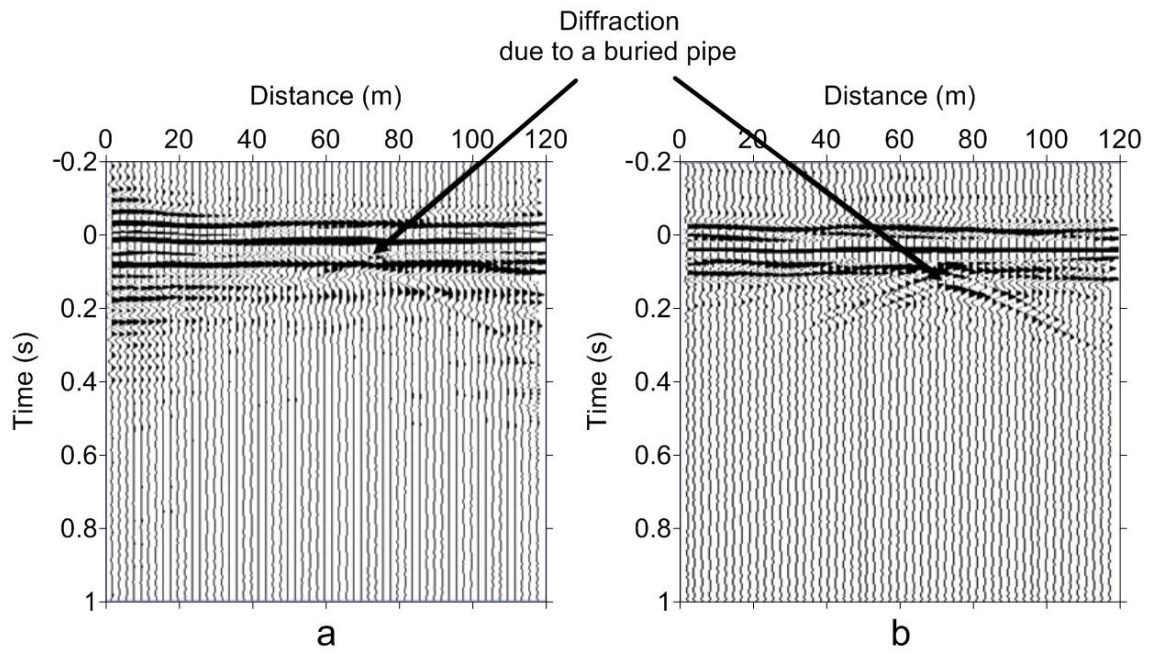
633

634 Figure. 5



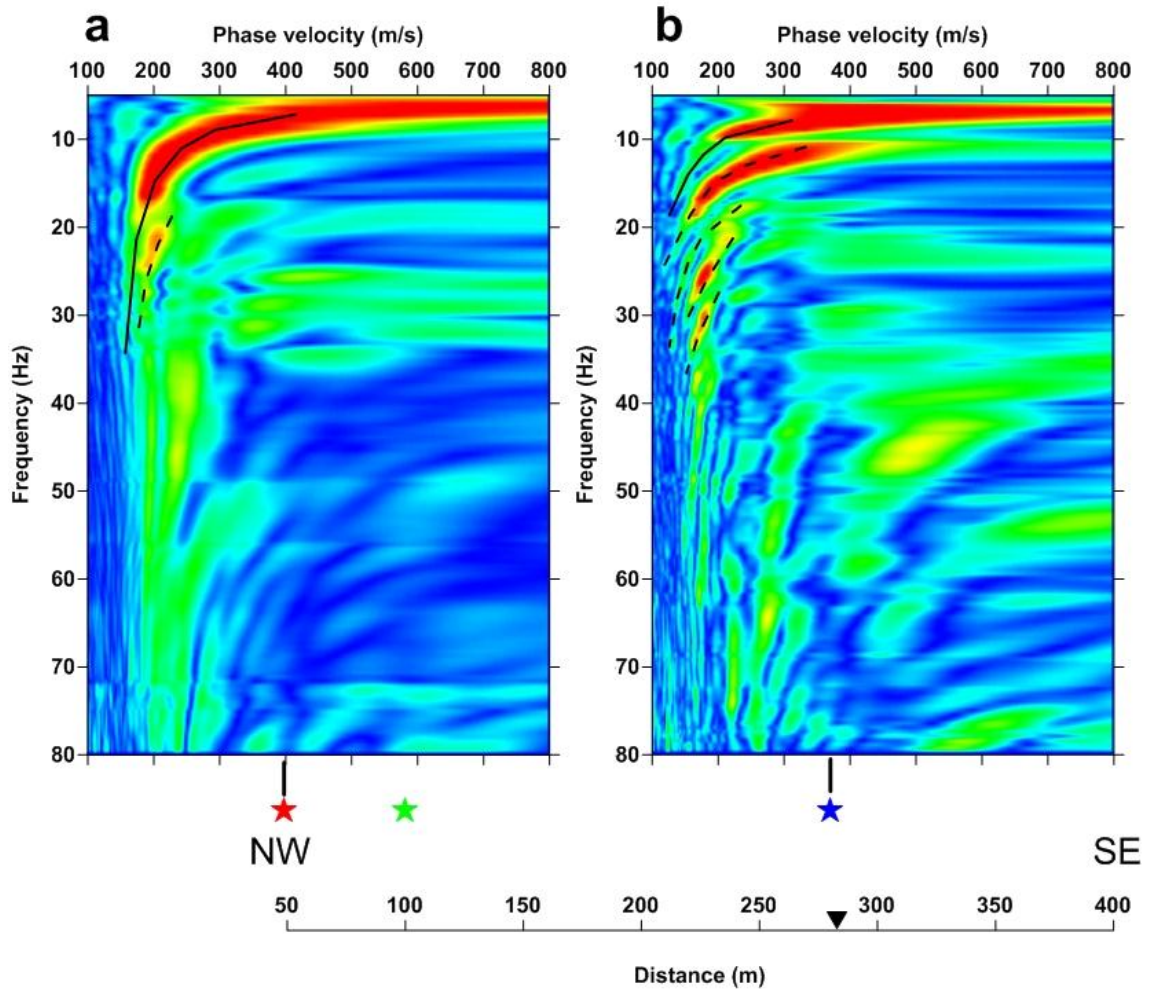
635

636 Figure. 6



637

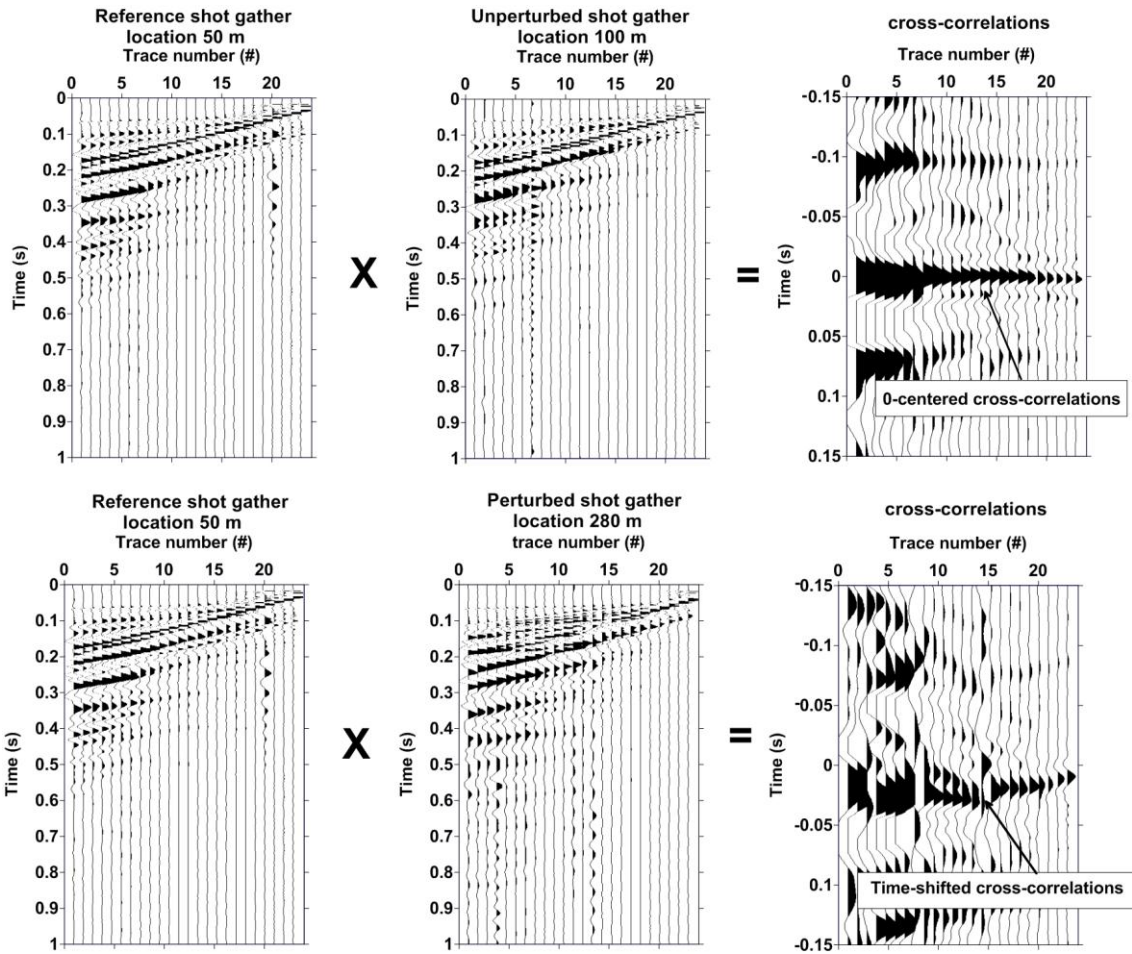
638 Figure. 7



- ★ Shot position of the reference gather shown in Fig. 9
- ★ Shot position of the non-perturbed gather shown in Fig. 9
- ★ Shot position of the perturbed gather shown in Fig. 9

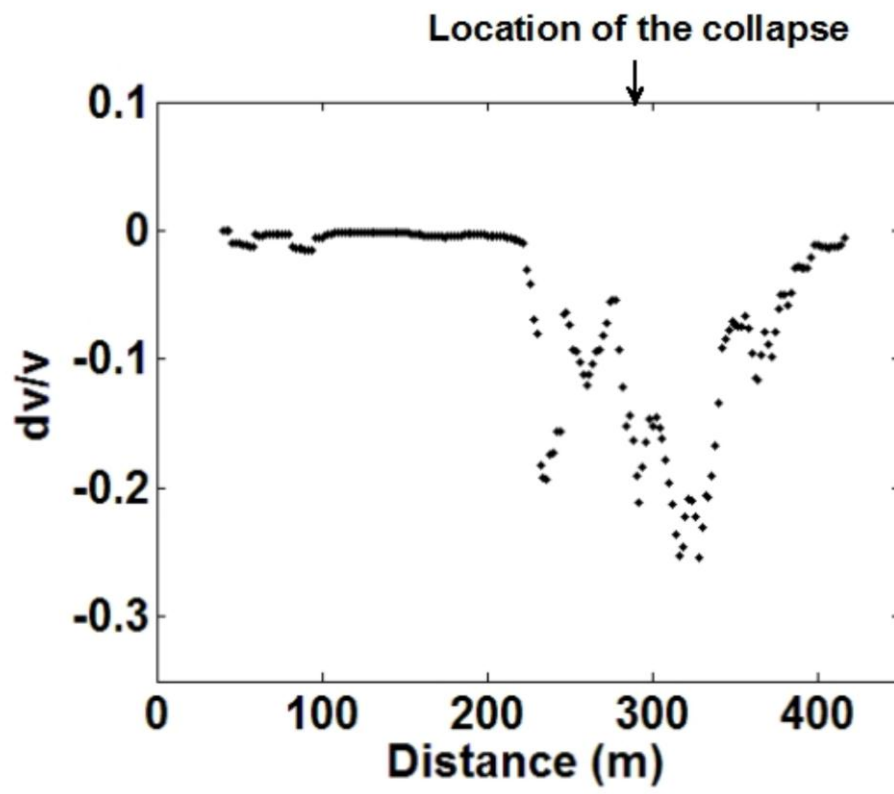
639

640 Figure. 8



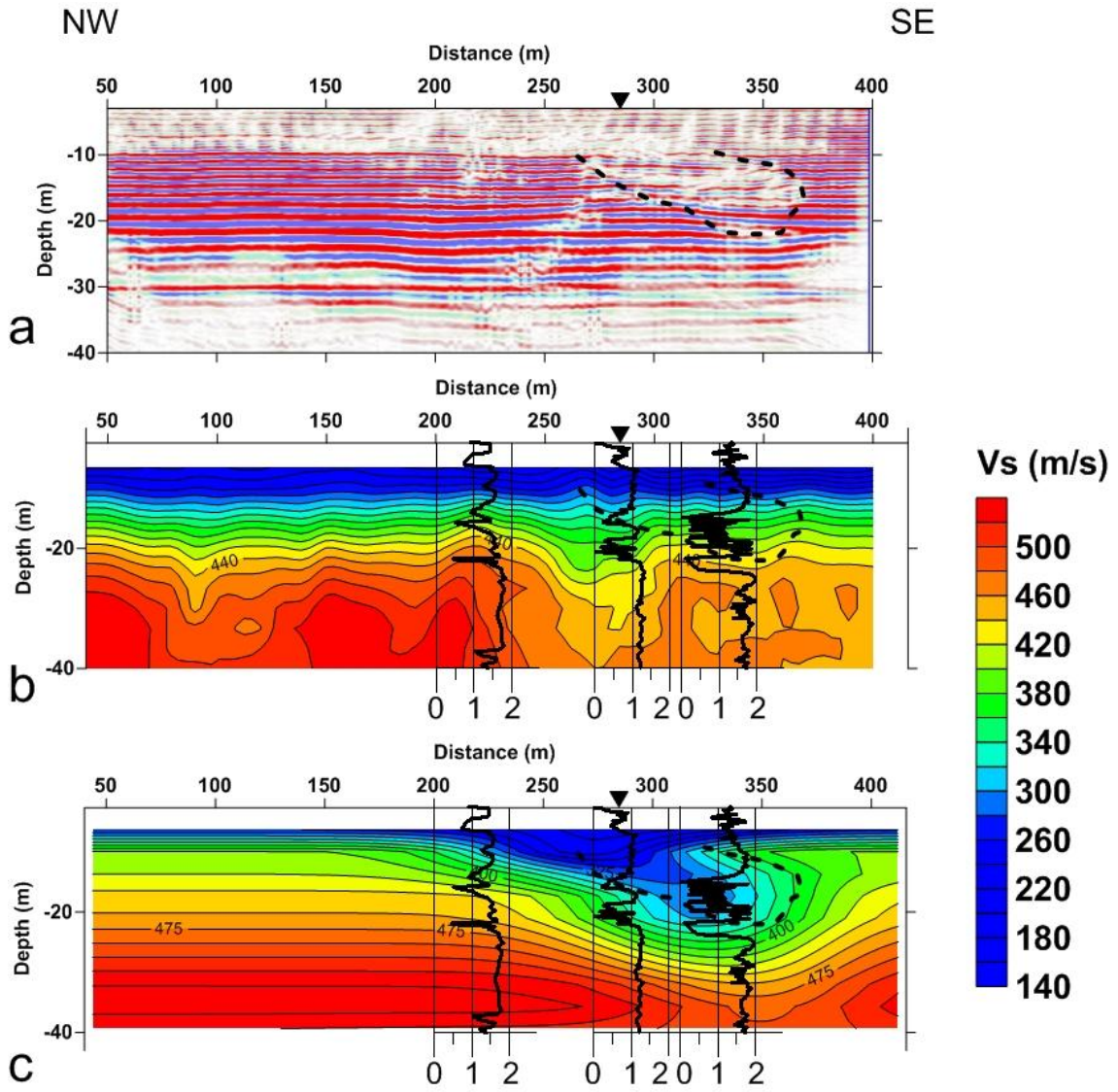
641

642 Figure. 9



643

644 Figure. 10



645

646 Figure. 11